Energy & Environmental Science

PAPER

View Article Online
View Journal | View Issue

Cite this: *Energy Environ. Sci.*, 2015, **8**, 1736

A quantitative analysis of the efficiency of solar-driven water-splitting device designs based on tandem photoabsorbers patterned with islands of metallic electrocatalysts†

Yikai Chen,‡[a] Ke Sun,‡[ab] Heather Audesirk,[b] Chengxiang Xiang*[a] and Nathan S. Lewis*[abcd]

Received 29th January 2015,
Accepted 23rd March 2015

DOI: 10.1039/c5ee00311c

www.rsc.org/ees

The trade-off between the optical obscuration and kinetic overpotentials of electrocatalyst films patterned onto the surface of tandem light-absorber structures in model photoelectrosynthetic water-splitting systems was investigated using a 0-dimensional load-line analysis and experimental measurements. The electrocatalytic performance of the catalyst at high current densities, normalized to the electrocatalyst surface area, is an important factor in the dependence of the optimal solar-to-hydrogen (STH) conversion efficiency, $\eta_{STH,opt}$, on the filling fraction (f_c) of the patterned catalysts, because even under conditions that produce minority-carrier current densities of $\sim$10 mA cm^{-2} at the solid/liquid interface, the current density at catalyst-bearing sites can be $>$1–2 A cm^{-2} in low filling-fraction films. A universal current-density *versus* potential relationship, up to current densities of 10 A cm^{-2}, was obtained experimentally for the hydrogen-evolution reaction (HER) using patterned Pt ultramicroelectrode (UME) arrays with a range of filling fractions and disc diameters. The $\eta_{STH,opt}$ of system designs that utilize patterned electrocatalysts located on the illuminated side of tandem photoabsorbers was then evaluated systematically. The maximum STH conversion efficiency, $\eta_{STH,max}$, using a hypothetical electrocatalyst that was optically transparent but which nevertheless exhibited a current-density *versus* potential behavior that is characteristic of the most active Pt films measured experimentally regardless of their optical obscuration, was 26.7%. By comparison, the maximum $\eta_{STH,opt}$ of 24.9% for real patterned Pt electrocatalyst films closely approached this ideal-case limit. The performance and materials utilization of the patterned electrocatalysts and of the uniformly coated electrocatalysts on tandem photoabsorbers were also compared in this study. Hence, patterned electrocatalysts with very low filling fractions can provide a potentially promising path to the realization of efficient large-scale photoelectrolysis systems while minimizing the use of scarce noble metals.

Broader context

Efficient photoelectrochemical water splitting requires the use of electrocatalysts that reduce the kinetic barriers to the reduction and oxidation half-reactions. However, the electrocatalysts can absorb or reflect light, and thus can limit the overall solar-to-hydrogen conversion efficiency. One strategy for reducing the optical obscuration that results from the presence of the electrocatalyst layer is to produce a patterned catalyst film that results in a low geometric filling fraction of the metal catalyst on the surface of the light absorbers, but reducing the filling fraction also increases the kinetic overpotentials required for the desired reactions. The systematic evaluation of a broad range of catalyst filling fractions and the influence of the fill fraction on the optimized design of a tandem solar-driven water-splitting system suggest that employing very low filling fractions of patterned electrocatalysts is a promising approach to the realization of efficient large-scale photoelectrolysis systems with minimized utilization of scarce noble metal electrocatalysts.

[a] *Joint Center for Artificial Photosynthesis, California Institute of Technology, Pasadena CA 91125, USA. E-mail: nslewis@caltech.edu, cxx@caltech.edu*
[b] *Division of Chemistry and Chemical Engineering, 210 Noyes Laboratory, 127-72, California Institute of Technology, Pasadena, CA 91125, USA*
[c] *Beckman Institute Molecular Materials Resource Center, California Institute of Technology, Pasadena, CA 91125, USA*
[d] *Kavli Nanoscience Institute, California Institute of Technology, Pasadena, CA 91125, USA*

† Electronic supplementary information (ESI) available. See DOI: 10.1039/c5ee00311c

‡ These authors contributed equally and are arranged alphabetically by last name.

I. Introduction

Key components of an efficient solar-driven water-splitting system generally include a tandem photoabsorber for efficient light collection and carrier transport, electrocatalysts for the hydrogen-evolution reaction (HER) and oxygen-evolution reaction (OER), and a membrane to separate the products.[1] The fabrication of a functioning integrated photoelectrode is more complex than simply identifying an optimally performing dark electrocatalyst and coating that catalyst onto the surface of a photoelectrode.[2–5] In general, the incident light must pass through the electrocatalyst, as well as through the electrolyte, to reach the tandem photoabsorber. Depending on the polarity of the tandem photoabsorber, the optical obscuration from either the HER catalyst or the OER catalyst coating can significantly alter spectrally, and/or attenuate the magnitude of, the incident illumination.[6] For planar electrode devices, the performance of a series of electrochromic metal oxide OER catalysts has been studied on an n-type photoanode with a band-gap energy, E_g, of 1.8 eV. Due to the loss of photocurrent produced by optical absorption by thick, but highly catalytic films, the maximal solar-to-hydrogen conversion efficiency, $\eta_{STH,max}$, was obtained using ultrathin catalyst films a few monolayers in thickness.[7]

One method to reduce the optical obscuration of the electrocatalyst layer is to produce a patterned catalyst film that results in a low geometric filling fraction of the metal catalyst on the surface of the light absorber (Scheme 1). The geometric filling fraction, f_c is defined as the ratio of the geometric area of the catalyst to the total geometric area of the photoelectrode. Moreover, for systems that utilize electrocatalysts based on precious metals, such as IrO_x for the OER and Pt for HER,[8] low-density patterning of the metal could provide significantly reduced materials usage of scarce elements relative to that required for planar, continuous films of electrocatalyst. However, at low f_c, the photocurrent will be concentrated into the area covered by the electrocatalyst film, and the high current densities through the electrocatalyst will require an additional overpotential to perform the interfacial electrochemical half-reaction of interest. The additional overpotential will, in turn, result in a reduction in the energy-conversion efficiency of the system. An analytical understanding of the trade-off between the reduction in photocurrent-density losses due to optical obscuration and the increase in catalytic overpotentials due to increased local operating current densities would therefore prove valuable for optimum-efficiency design of an integrated planar-photoelectrode water-splitting system. The analysis of the efficiency of device designs based on patterned metal catalysts is complicated by considering that the increased overpotential can be partially compensated for by reoptimization of the band gaps of the tandem light absorbers onto which the patterned electrocatalysts are deposited, to thereby utilize a different set of light absorbers that provide an increased operating voltage to effect the water-splitting reaction at optimal system efficiency. However, the increase in band gaps in the altered light absorbers will also produce a decrease in photocurrent due to a less optimal match of the spectral absorption of the light absorbers with the incident solar illumination. Additionally, at very low filling fractions of metal, the current density at the electrocatalyst can approach or exceed 1 A cm^{-2}, at which point mass-transport effects can become limiting except in specific geometries such as devices that exploit radial diffusion to small islands of metallic electrocatalysts. Hence the solar-to-hydrogen efficiency attainable in an optimally designed integrated tandem-photoabsorber system with patterned metal electrocatalysts, $\eta_{STH,opt}$, is dependent on the band-gap combinations of the photoabsorbers, the current–voltage characteristics of the absorbers and electrocatalysts, the optical properties and filling fraction of the electrocatalyst films, and the transport in the solution electrolyte.

To analyze quantitatively the trade-offs involved with this set of mutually interdependent effects, the electrochemical and optical properties of patterned Pt catalysts with different filling fractions on crystalline Si substrates has been investigated herein. The patterned Pt catalysts behaved as arrays of ultramicroelectrodes (UMEs), in which, due to radial diffusion, the limiting current density at the patterned microelectrodes was many orders of magnitude higher than that obtainable using a continuous film in a planar electrode geometry. The electrochemical behavior of this system has revealed the intrinsic HER kinetic properties of Pt at high current densities. In addition, the optical and catalytic properties of planar and patterned metallic electrocatalysts have been investigated at different thicknesses of the metal film and at different filling fractions. These experimental parameters were then used in a one-dimensional multiphysics model that accounted for the performance of a

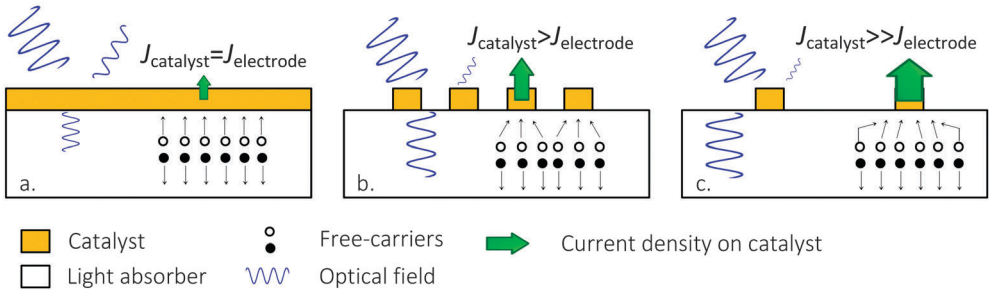

Scheme 1 Schematic illustration of the trade-offs between optical obscuration and concentrated operational current densities at the catalyst surface for photoabsorbers (a), coated with continuous electrocatalyst films; (b) coated with patterned electrocatalyst films with high filling fractions, and (c) coated with patterned electrocatalyst films with low filling fractions.

tandem photoabsorber, the obscuration and activity of a patterned electrocatalyst film, and the transport properties of a membrane and liquid electrolyte, to explore the trade-space for water-splitting systems that employ tandem photoabsorbers patterned with arrays of electrocatalysts.

II. Experimental methods and modeling approaches

A. Preparation of patterned electrocatalyst films

Pt UME arrays were patterned on planar, degenerately As-doped (<0.005 ohm cm), Si(111) (n^+-Si) substrates. In this process, AZ® nLOF 2020 photoresist was spin-coated onto an HF-cleaned Si surface at 2000 rpm for 1 min. The photoresist was baked at 110 °C for 1 min, exposed to light for 9.5 s, and then baked at 110 °C for 1 min. For light exposure through a contact mask, the samples were developed using AZ® 300 MIFdeveloper for 90 s, and the photolithographic process was completed by a thorough rinse with deionized H_2O. After etching for 10 s in buffered HF, the samples were immediately loaded into a sputtering system (AJA) with a base pressure of 3×10^{-8} Torr. An intermediate layer of Ti (20 nm) was deposited to enhance the adhesion of the electrocatalyst films. Pt was then sputtered at a deposition rate of 0.1 nm s^{-1}, with various sputtering times producing different Pt film thicknesses. Ultrasonication at low power (<15 W) assisted the lift-off on diced samples. The samples were then rinsed with isopropanol and dried under a stream of N_2(g). The measured filling fraction of the patterned catalyst microelectrode produced by the photolithography process was larger than the design on the photomask because the broad-spectrum ultraviolet light used during the photolithographic process resulted in the diameter of each Pt dot being $\sim$21% larger (6.0 ± 0.3 μm) than the design on the chrome mask (5 μm).

After the Pt UME arrays were patterned, the thickness of the metal was measured by atomic-force microscopy (AFM) and scanning-electron microscopy (SEM). SEM imaging was performed using a Nova NanoSEM 450 (FEI) with an accelerating voltage of 5 kV. AFM images of an n^+-Si|Pt UME array with a Pt thickness of 2 nm were collected using a Bruker Dimension Icon microscope operating in ScanAsyst mode and using Bruker ScanAsyst-Air probes (silicon tip on a silicon nitride cantilever, spring constant: 0.4 N m^{-1}, frequency: 50–90 kHz, Al back coating). The scan size was ~ 5 μm $\times$ 5 μm. The images were analyzed using NanoScope software version 1.5 and flattening was performed during image processing to remove curvature and slope from the images.

Ohmic contacts to the electrodes were formed by scribing an In–Ga eutectic alloy (Alfa Aesar, 99.99%) onto the back side of the n^+-Si samples, respectively. The resulting ohmic contact was mechanically attached with high-purity Ag paint (SPI supplies) to a coiled, tin-plated Cu wire (McMaster-Carr), which was then threaded through a glass tube (Corning Incorporation, Pyrex tubing, 7740 glass). The sample was encapsulated and sealed to the glass tube using a mixture of 2 : 1 grey epoxy (Hysol 9460F) and white epoxy (Hysol 1C). The epoxy was allowed to dry under ambient conditions for >12 h. The exposed surface area of each electrode was imaged with a high-resolution optical scanner (Epson perfection V370 with a resolution of 2400 psi), and the geometric areas were determined by analyzing the images using ImageJ software. All of the electrodes in this study were 0.1–0.2 cm^2 in area, unless specified otherwise.

B. Optical and electrochemical characterization

The optical absorption of Pt-coated Si samples was determined by use of an integrating sphere at normal incidence (Agilent Cary 5000 UV-Vis spectrometer). The absorption of Si coated with a Pt UME array was determined by subtracting the measured reflection and transmission from unity.

The optical dispersion properties of the thin Pt films (2–80 nm) were characterized using a variable-angle spectroscopic ellipsometer with a rotating analyzer and equipped with an autoretarder (J.A. Woollam Co., Inc.). Measurements were performed with 0.025 eV steps in the 0.5–4.5 eV spectral range and for incidence angles between 65° and 75°. A general oscillation model containing Gaussian and Lorentzian oscillators was used to fit the ellipsometry data and to obtain physically reasonable optical dispersion properties of the thin metal layers.

For electrochemistry, a silver/silver chloride (Ag/AgCl in 1.0 M KCl(aq), CH Instruments, CH152) electrode was used as the reference electrode, and a carbon cloth placed within a fritted glass tube (gas dispersion tube Pro-D, Aceglass, Inc.) was used as the counter electrode. All electrochemical measurements were performed in a pre-electrolyzed 1.0 M H_2SO_4(aq) solution.[9] The Ag/AgCl reference electrode was calibrated *versus* a reversible hydrogen electrode (RHE), with the Ag/AgCl electrode potential determined to be 0.26 V *vs.* RHE. A custom electrochemical cell with a flat glass (Pyrex) bottom was used for all of the electrochemical measurements. Before measurement, the electrolyte was purged for >30 min with 1 atm of high-purity (99.999%) H_2(g). Once the equilibrium potential had been reached, the potential was monitored using a polished and cleaned reversible Pt working electrode (CHI102) at open circuit. During the measurements, the electrolyte was continuously purged with 1 atm of high-purity H_2(g), to ensure that the electrolyte was continuously saturated with H_2(g). The electrolyte was vigorously agitated with a magnetic stir bar that was driven by a model-train motor (Pittman) in conjunction with a Railpower 1370 speed controller (Model Rectifier Corporation). The reported aqueous electrochemical measurements do not include compensation for series resistance.

Cyclic voltammetry was obtained using a Biologic SP-200 potentiostat (Bio-Logic Science Instrument). The cyclic voltammetric data were recorded at a scan rate of 40 mV s^{-1}.

The resistance loss in the Pt/Ti/Si layers was measured on solid-state devices. Patterned front contact pads (20 nm Ti/30 nm Pt) with diameters of 1 mm and InGa eutectic back contacts were employed in the measurements. The total resistance in the layers was dominated by the Ti/Si contact resistance

and was in the range of $\sim 0.01\ \Omega\ \mathrm{cm}^{-2}$. All of the current-voltage relations and the subsequent numerical calculations presented herein were corrected for resistance losses.

C. Modeling and simulation

a. Modeling η_{STH} with a 0-dimensional load-line analysis. The STH conversion efficiency, η_{STH}, was calculated using eqn (1):

$$\eta_{STH} = \frac{1.23(\mathrm{V}) \times J_{op}(\mathrm{mA\ cm^{-2}})}{S(\mathrm{mW\ cm^{-2}})} \quad (1)$$

where J_{op} is the operating photocurrent density ($\mathrm{mA\ cm^{-2}}$) and S is the total incident solar irradiance ($\mathrm{mW\ cm^{-2}}$). The value of J_{op}, as well as the corresponding operating voltage, V, can be represented by the cross-section of the diode curve for the light absorber in conjunction with the loading curve, which is indicative of the performance of the electrocatalyst as well as the solution conductivity.

Shockley–Queisser limit for light absorbers. The ideal limiting case, *i.e.* the Shockley–Queisser (S–Q) limit, in which the current–voltage relationship for a tandem photoabsorber is determined by use of a detailed-balance calculation, is obtained when the current density at the operating photovoltage is equal to the sum of the incident solar radiation (J_{ph}) and the thermal radiation (J_{th}) minus the radiative emission (J_{rad}):

$$J = J_{ph} + J_{th} - J_{rad} \quad (2)$$

J_{ph}, J_{rad} and J_{th} were determined by:

$$J_{ph} = e\int_{E_g}^{\infty} d\hbar\omega \frac{\Lambda(1-f_c)}{\hbar\omega}, \quad (3)$$

$$J_{rad} = \frac{e\left(n_{top}{}^2 + n_{bottom}{}^2\right)}{4\pi^2 c^2}\int_{E_g/\hbar}^{\infty} d\omega\omega^2 \exp\left(\frac{eV-\hbar\omega}{kT}\right), \quad (4)$$

and

$$J_{th} = \frac{e\left(n_{top}{}^2 + n_{bottom}{}^2\right)}{4\pi^2 c^2}\int_{E_g/\hbar}^{\infty} d\omega\omega^2 \exp\left(-\frac{\hbar\omega}{kT}\right). \quad (5)$$

In eqn (3)–(5), e is the unsigned charge on an electron, Λ is the wavelength-dependent solar flux in the Air Mass (AM)1.5 solar spectrum, f_c is the filling fraction of the catalysts, $\hbar$ is Planck's constant divided by 2π, ω is the frequency of the incident light, n_{top} and n_{bottom} are the refractive indices of the top and the bottom of the tandem absorber, respectively, T and V are the operating temperature and the operating voltage, respectively, and E_g is the band gap of the top or bottom light absorber, as indicated by the appropriate subscript. As shown in eqn (3), no transmission was assumed in the catalyst-covered region and 100% transmission was assumed in the exposed region.

Behavior of electrocatalysts, membrane separator and solution electrolyte. The current density, $J_{OER/HER}$ as a function of the overpotential, η, for the OER and HER can be described by the Butler–Volmer equation:

$$J_{OER/HER} = J_{0,OER/HER}\left[\exp\left(\frac{\alpha_{a,OER/HER} e\eta}{kT}\right) - \exp\left(-\frac{\alpha_{c,OER/HER} e\eta}{kT}\right)\right], \quad (6)$$

where $J_{0,OER/HER}$ is the exchange-current density for the OER or HER, respectively, and $\alpha_{a,OER/HER}$ and $\alpha_{c,OER/HER}$ are the anodic and cathodic transfer coefficients, respectively, for the OER or the HER. Note that for the catalyst films comprised of patterned disks, the current density at each disk is $1/f_c$ greater than that for planar catalyst films.

For a zero-dimensional (0-D) analysis of the STH conversion efficiency, the value of the operating current density as well as the corresponding operating voltage, V, can be represented by the cross-section of the diode curve for the light absorber in conjunction with the loading curve, which is indicative of the performance of the electrocatalyst as well as the solution and membrane conductivity. The electrode surfaces were assumed to be isopotential surfaces, and the spatial inhomogeneity of the current-density distribution along the electrodes was approximated by the use of a 0-D effective transport resistance.

For every specific filling fraction, OER performance, and HER catalytic performance, the 0-D analysis was performed with each band-gap combination, to calculate the optimal STH conversion efficiency. In general, when the catalyst loading increased, re-optimization of the band gaps of the tandem structure allowed for the design of a system with a much higher system efficiency than the system efficiency obtained by fixing the properties of the tandem structure based on negligible system losses.

b. Modeling the mass transport in patterned electrocatalyst films

Ion transport in the bulk. For species i, the general mass balance for the diluted species in the electrolyte was described by the Nernst–Planck equation under a steady-state assumption,

$$\nabla\cdot(-D_i\nabla c_i - z_i u_{m,i} F c_i \nabla\phi_l + c_i\vec{u}) = 0, \quad (7)$$

where c_i represents the concentration of the ion i, z_i, D_i, $u_{m,i}$ represent the valence, diffusion coefficient, and mobility, respectively, of the ion, F is Faraday's constant, ϕ_l is the electrolyte potential, and $\vec{u}$ is the velocity vector. The concentration of HSO_4^- was computed from the electroneutrality condition, which ensured that the net charge was zero. Convection was neglected in the calculations described herein.

The diffusion coefficient was related to the mobility by the Nernst–Einstein relation,

$$u_{m,i} = \frac{D_i}{RT} \quad (8)$$

Behavior of electrocatalysts. The concentration of the oxidant and of the reductant, respectively, at the catalyst/electrolyte interface impacts the relationship between the current density and overpotential represented by the Butler–Volmer equation.

The relationship can be modified as follows:

$$J_{\mathrm{HER}} = J_{0,\mathrm{HER}}\left[\frac{C_{H_2}}{C_{H_2,e}}\exp\left(\frac{\alpha_{a,\mathrm{HER}}e\eta}{kT}\right) - \frac{C_{H^+}}{C_{H^+,e}}\exp\left(-\frac{\alpha_{c,\mathrm{HER}}e\eta}{kT}\right)\right], \quad (9)$$

where $J_{0,\mathrm{HER}}$ is the exchange-current density, $\alpha_{a,\mathrm{HER}}$ and $\alpha_{c,\mathrm{HER}}$ represent the anodic and cathodic transfer coefficients, respectively, C_{H_2} and C_{H^+} are the respective hydrogen and ion concentrations at the interface, and $C_{H_2,e}$ and $C_{H^+,e}$ are the corresponding equilibrium concentrations of the indicated species. Constants used in the calculation are listed in Table S1.

The overpotential, η, was defined as:

$$\eta = \phi_s - \phi_l - \phi_0 \quad (10)$$

where ϕ_s and ϕ_l are the electric and electrolyte potential at the electrode–electrolyte interface, respectively, and ϕ_0 is the equilibrium potential. The value of ϕ_0 was set to ϕ_0 = 0.0 V. Conservation of charge and continuity of current density were stipulated at the electrode/catalyst interface. A fixed proton concentration (1 M) at the boundary layer and the modified Butler–Volmer equation were used as the boundary conditions for this model.

III. Results

A. HER at Pt Ultramicroelectrodes

Fig. 1 shows SEM images of patterned Pt UME arrays on n^+-Si substrates. The photolithographic lift-off process produced uniform Pt UME arrays with a diameter of 6.0 ± 0.3 μm and with a pitch of 50 μm to 8.3 μm, depending on the mask used in the lithographic process. The resulting filling fractions of the patterned films therefore varied from 0.011 to 0.473 based on the ratio of the area covered by the Pt to the total geometric area of the Si substrate, including the area covered by Pt.

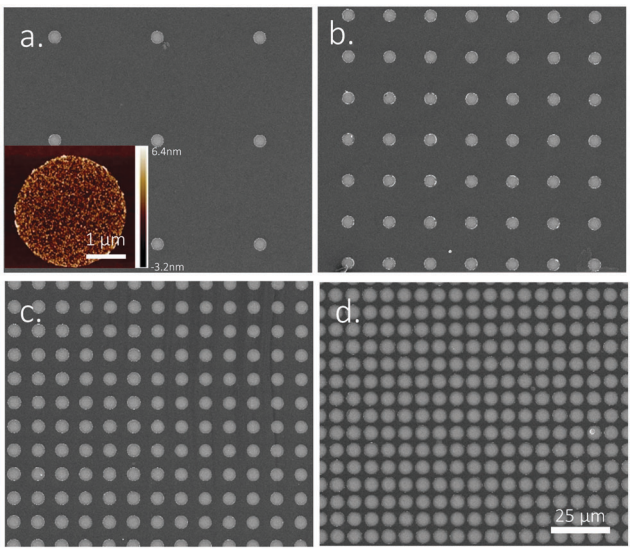

Fig. 1 Scanning-electron microscopy images of patterned Pt films with a thickness of 2 nm, a diameter of 6.0 ± 0.3 μm, and with an actual catalyst filling fraction, f_c, of (a) 0.011 ± 0.002, (b) 0.063 ± 0.004, (c) 0.216 ± 0.007 and (d) 0.473 ± 0.010, respectively. The inset is a high-resolution AFM image of a single disc with a diameter of 3 μm.

The electrocatalytic activity of the Pt as a function of thickness, were studied using an unpatterned film of Pt on an n^+-Si substrate, with an intermediate Ti layer (20 nm) for improved adhesion. Fig. 2a shows the geometric current density ($J_{\mathrm{electrode}}$) *versus* potential (E) behavior for n^+-Si|Ti|Pt electrodes with the Pt thickness varying from 1 to 10 nm. The HER catalytic activity of the Pt film was essentially unchanged when the nominal film thickness was ≥2 nm. For films with a nominal Pt thickness ≥ 2 nm, the extracted exchange-current densities (J_0) based on a Tafel fit in the cathodic current-density range of 1–10 mA cm^{-2} were ~0.99 ± 0.01 mA cm^{-2}, and the corresponding Tafel slopes were ~22.5 ± 1.1 mV dec^{-1}. The overpotential needed to obtain a current density of −10 mA cm^{-2} remained constant (−24 ± 1.5 mV) for films with a nominal Pt thickness ≥ 2 nm but increased in magnitude to −50 ± 3.5 mV for samples having a nominal Pt film thickness of 1 nm. Moreover, samples with a nominal Pt thickness of <2 nm showed a slow degradation in their performance over a few cyclic voltammetric scans, presumably due to insufficient catalyst loading and the delamination caused by high normalized current densities at the regions of the surface that were coated with the electrocatalyst. AFM measurements showed that a 2 nm Pt film deposited directly on Si, without a Ti adhesion layer, was not continuous and had a roughness (1.53 nm) comparable to the film thickness (Fig. 1a inset).

The optical dispersion properties of ultrathin Pt catalysts were studied using spectroscopic ellipsometry (Fig. S1, ESI†). The properties of bulk Pt cannot be used to describe the optical constants of ultra-thin films, so the ellipsometric data for crystalline Si substrates that were covered with native oxides (2 nm) were fitted using a general oscillation model to ensure that the resulting optical constants retained a physically reasonable shape. Obtaining a good fit when the film was thinner than 2 nm required the inclusion of surface roughness consistent with the AFM data (Fig. S1a and b, ESI†). Because the film morphology and structure were affected by the film thickness, the optical properties were a function of the thickness until the film became completely opaque, when the thickness was >80 nm, the thickest film studied in our case (Fig. S1c and d, ESI†). The optical transmittance and reflectance of Pt films deposited on Si and on quartz substrates were measured using UV-vis spectroscopy. Increases in the thickness of the Pt film reduced the transmittance (~85% to ~30%) and increased the total reflectance (~10% to ~36%) on quartz substrates. Due to the increased extinction coefficient (k) in addition to the increased film thickness, the absorptance also increased (<5% to ~30%, Fig. S2c, ESI†). The use of an adhesion layer (20 nm Ti film in this experiment) with a 2 nm Pt film further reduced the optical transmission to ~20% (black curve in Fig. S2a, ESI†). Moreover, increasing the film thickness on Si also increased the reflectance. However, the reflectance in the wavelength range of 350–600 nm was smaller for a 2 nm Pt-coated Si substrate with

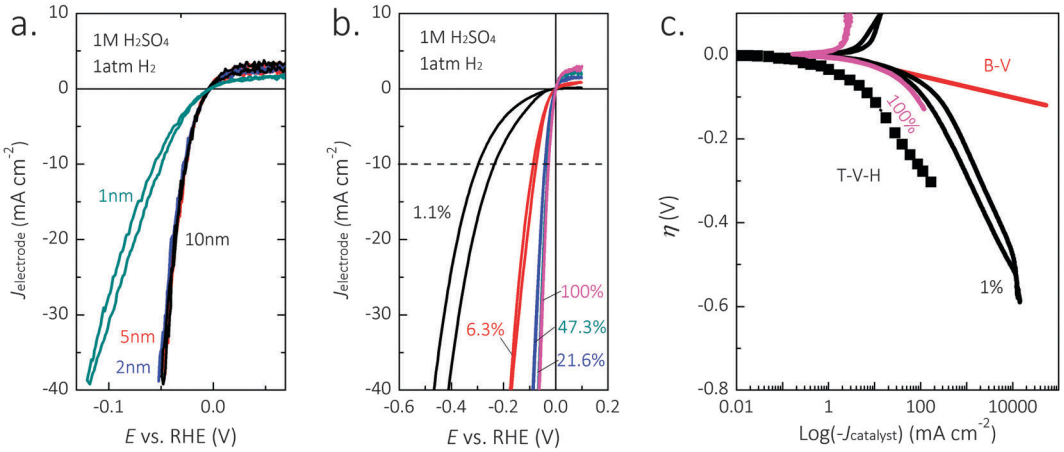

Fig. 2 Geometric current density ($J_{electrode}$) as a function of the applied potential for Pt films with different thicknesses (a) and patterned Pt films with different filling fractions (b). (c) Kinetic overpotential as a function of the normalized current density ($J_{catalyst}$) at different filling fractions in comparison with the Butler–Volmer (B–V) and the Tafel–Volmer–Heyrovsky (T–V–H) models (data were extracted from ref. 10). All data were corrected for resistance losses.

an intermediate Ti layer than the reflectance measured for a 2 nm Pt film deposited directly on Si. This behavior was due to the lower refractive index of Ti relative to Si, and due to the structure/thickness of the Ti adhesion layer, which can be considered as a bulk substrate.

The *J–E* behavior of the patterned Pt UME arrays with different diameters and filling fractions of the Pt UME array was characterized experimentally on n^+-Si dark electrodes. Fig. 2b plots the current density with respect to the total geometric electrode surface area, $J_{electrode}$, of the Pt and Si combined, as a function of the applied potential for the HER. As the filling fraction of the Pt UME array decreased, a decrease in the concentration-limited current density for H_2 oxidation was observed at positive potentials. This behavior is in accord with expectations for a reduction in the catalytically active surface area as the Pt filling fraction decreased. In the current density range ($-J_{electrode}$) of 1 to 10 mA cm^{-2}, the Tafel slope increased as f_c decreased. A reduction in f_c therefore produced an increase in the magnitude of the overpotential required to obtain a current density of 10 mA cm^{-2}. However, the exchange-current densities obtained from the Tafel fitting were unaffected by a reduction in the f_c of the Pt. Table 1 summarizes the dependence of the Tafel slope, the geometric exchange-current density, and the overpotential on the value of f_c for the Pt UME arrays investigated.

Fig. 2c presents the kinetic overpotential as a function of the normalized current density, $J_{catalyst}$, based only on the area covered by the Pt, at different filling fractions of the Pt UME array on Si. All of the curves matched well, especially at low values of $J_{catalyst}$. At high values of $J_{catalyst}$, the patterned Pt UME-array electrodes with low filling fractions showed higher turnover-limited current densities than did the Pt UME arrays at high filling fraction. A universal electrocatalytic curve for the HER behavior was therefore observed for $-J_{catalyst}$ up to 10 A cm^{-2} in low filling-fraction films. As shown in Fig. 2c, the universal electrocatalytic curve could not be fitted to a simple Butler–Volmer (B–V) Tafel relation with a single exchange-current density and Tafel slope (red curve). Instead, in low current-density regions ($-J_{catalyst} < 10$ mA cm^{-2}), the fitted Tafel slope was 23 mV dec^{-1} and in high current-density regions ($-J_{catalyst} > 50$ mA cm^{-2}), the fitted slope was 180 mV dec^{-1}.

The standard Butler–Volmer equation does not provide an adequate description for the HER.[10] Two-step kinetic descriptors (including Volmer–Hyrovsky, Volmer–Tafel, or Heyrovsky–Tafel) have been developed to describe the HER in limited potential ranges. The kinetics of the HER at steady state are generally and more accurately described through three elementary steps, denoted as Tafel (T), Volmer (V), and Heyrovsky (H), respectively:

$$H_2^m + 2m \overset{T}{\longleftrightarrow} 2H_{ad} \quad (11)$$

$$H_{ad} \overset{V}{\longleftrightarrow} H^+ + e^- + m \quad (12)$$

$$H_2^m + m \overset{H}{\longleftrightarrow} H_{ad} + H^+ + e^- \quad (13)$$

where m is the active site, H_2^m is the molecular hydrogen at the electrode surface, H_{ad} is the adsorbed hydrogen atom, and H^+ is a proton. Two-step mechanisms may dominate at different overpotential ranges, which is consistent with the two different slopes observed for the universal electrocatalytic curve.

Table 1 Tafel slope, exchange-current density, and overpotential as a function of filling fraction (f_c)

	$f_c = 1.00$	$f_c = 0.473$	$f_c = 0.216$	$f_c = 0.063$	$f_c = 0.011$
Tafel slope (mV dec^{-1})	22.5 ± 1.1	34.6 ± 1.4	39.2 ± 1.9	67.7 ± 2.5	233.0 ± 2.8
Exchange-current density (mA cm^{-2})	−0.99 ± 0.01	−1.01 ± 0.01	−0.99 ± 0.01	−0.99 ± 0.01	−1.00 ± 0.01
Overpotential (mV) at $J_{electrode} = -10$ mA cm^{-2}	−24.0 ± 1.5	−30.4 ± 0.2	−39.0 ± 2.0	−66.5 ± 8.5	−193.5 ± 50.5

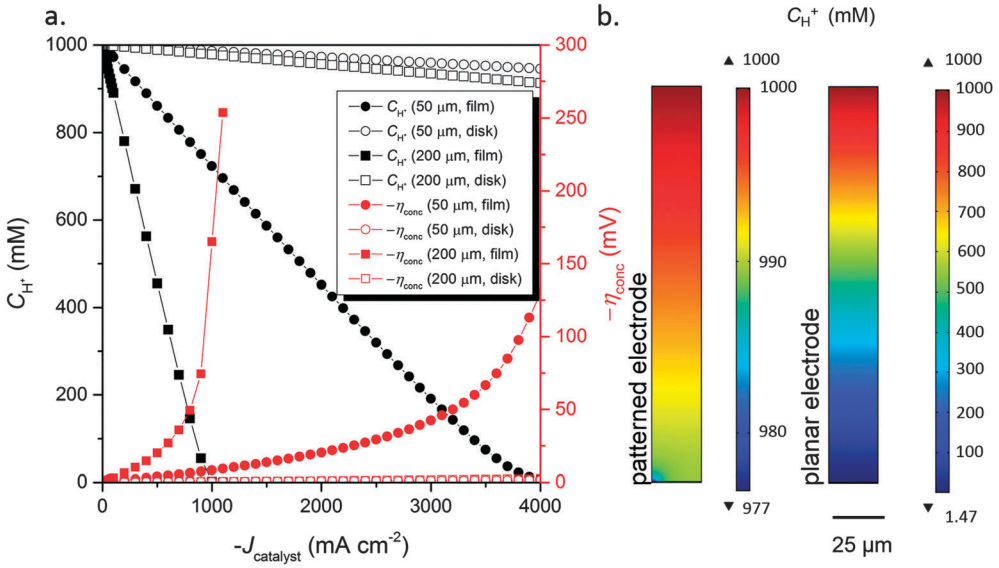

Fig. 3 (a) Proton concentration at the electrode surface (left axis) and concentration overpotential (right axis) as a function of the normalized current densities of a planar electrode (solid) and of a patterned electrode (hollow) with a disc diameter of 5 μm and a filling fraction of 1%. (b) Proton-concentration profile in a patterned UME-array electrode (left) and in a planar electrode (right).

Fig. 2c compares the *J*–*E* relationships of the patterned Pt film and the planar Pt electrode with the Butler–Volmer (B–V) model and with the Tafel–Volmer–Heyrovsky (T–V–H) model.[10] Table S2 summarizes the f_c independent Tafel slope, exchange current density, and overpotential based on the normalized current density ($J_{catalyst}$).

B. Mass transport at planar and ultramicroelectrodes

Measurement of the intrinsic electrochemical kinetics at high current densities is difficult using a macroscopic planar electrode, due to the concentration-overpotential loss and the resistive loss.[11] However, the patterned electrocatalyst films behaved as UME arrays, and thus provided a platform for studying the electrochemical interfacial kinetics of water-splitting half-reactions at high current densities, without complications due to significant mass-transport limitations.[11,12] Fig. 3a shows the simulated proton concentration at the surface of the electrode, and the corresponding concentration overpotential, η_{conc}, as a function of $J_{catalyst}$ for a planar electrode and for a patterned Pt electrocatalyst film, respectively. For the planar electrodes, η_{conc} was significant at high current densities, especially when the hydrodynamic boundary layer was large. For instance, when the thickness of the hydrodynamic boundary layer was set to 200 μm, the proton concentration at the surface of the planar electrode approached 0 mM near $-J_{catalyst}$ = 1000 mA cm^{-2} (black solid square curve), which resulted in a significant increase in the magnitude of η_{conc}, as follows from eqn (9). In contrast, due to radial diffusion, the performance of the patterned electrocatalyst film showed minimal concentration-overpotential loss and was independent of the thickness of the hydrodynamic boundary layer. At $-J_{catalyst}$ = 1 A cm^{-2}, for Pt islands with a diameter of 5 μm and f_c = 0.010, the proton concentration at the electrode surface remained close to the concentration in the bulk solution, and the corresponding overpotential was $-\eta_{conc} < 1$ mV (Fig. 3b). At high current densities, the decrease in the proton concentration at the surface of planar electrodes causes significant concentration-overpotential losses for the HER. In contrast, radial diffusion at UMEs enhances the limiting current by several orders of magnitude and therefore minimizes the concentration overpotential under such conditions.

C. Calculated optimal STH conversion efficiency for tandem light absorbers coated by uniform electrocatalyst films and patterned electrocatalyst films

When the light is incident on the catalyst-bearing side of the photocathode in a tandem photoabsorber, with the photocathode coated with a uniform Pt film, $\eta_{STH,opt}$ considering all band-gap combinations was calculated to be 24.4% and 22.6% for a nominal Pt thickness of 1 nm or 2 nm, respectively. In these calculations, the tandem photoabsorber was assumed to operate at the Shockley–Queisser (S–Q) limit and the performance of a state-of-the-art OER catalyst was used for the photoanode side of the device, whereas the electrocatalytic performance exhibited in Fig. 1 was used for the light-facing cathode side of the tandem structure.

Fig. 4a shows $\eta_{STH,opt}$ at all band-gap combinations as a function of the filling fraction of the Pt electrocatalyst film. The experimentally determined *J*–*E* relationship of a patterned Pt film with f_c = 0.010 (Fig. 2b, black curve) was used in the calculation. The 2 nm thickness of Pt was used primarily to produce a saturated catalytic activity on a planar non-patterned substrate, while reducing the use of precious metal. The activity on patterned substrates therefore only depended on the filling fraction of the catalysts and was independent of the thickness as long as the film is ≥2 nm. Although 2 nm Pt did not result in an optically opaque film (Fig. S2, ESI†), an adhesion layer is

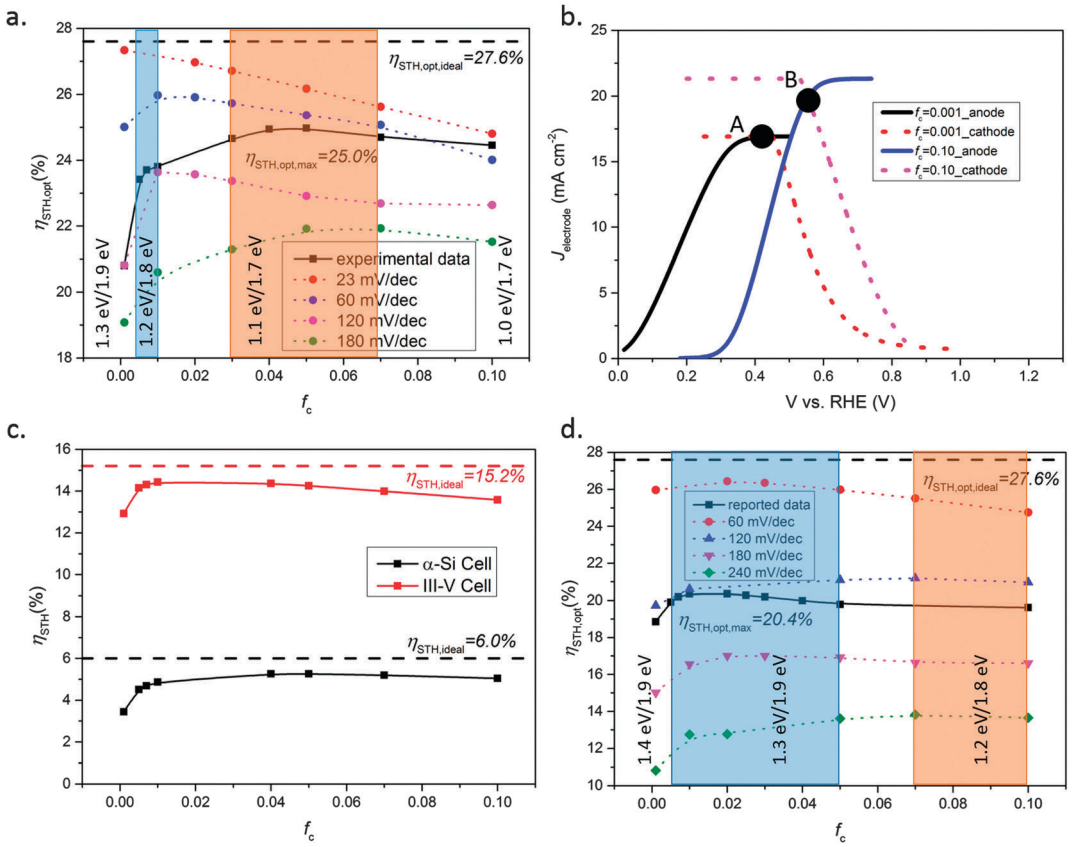

Fig. 4 (a) Optimal solar-to-hydrogen conversion efficiency, $\eta_{STH,opt}$, considering all band-gap combinations at the Shockley–Queisser limit as a function of the Pt filling fraction for four different Tafel slopes (dotted curves) and for the experimental current-density *versus* potential (*J*–*E*) relationship after correction for resistance (solid black curve). The maximum attainable efficiency, $\eta_{STH,max}$ = 27.6%, calculated using the experimental electrocatalytic behavior of thick continuous Pt films in the absence of any optical obscuration, is indicated by the dashed horizontal line. (b) Analysis of the operating current density of solar-driven water-splitting devices based on a photocathode-plus-photoanode analysis for f_c equal to 0.001 (point A) and 0.1 (point B). (c) η_{STH}, as a function of the Pt filling fraction for the experimental *J*–*E* relationship for a triple-junction a-Si:H cell (black) and a triple-junction III–V cell (red). The dotted horizontal lines indicate the maximum attainable efficiencies, $\eta_{STH,max}$, without assuming any optical obscuration but assuming the performance of the Pt electrocatalyst film determined experimentally in this study and assuming state-of-the-art electrocatalyst behavior for the oxygen-evolution reaction (OER). (d) Calculated $\eta_{STH,opt}$ considering all band-gap combinations at the Shockley–Queisser limit as a function of the filling fraction of the OER catalyst for four different Tafel slopes (dotted curves) and for the reported *J*–*E* relationship (black curve).

typically needed and was actually used in our experiment (20 nm Ti metal), which resulted in a nearly opaque film (Fig. S2, ESI†). Therefore, the computational model assumed that no light was transmitted to the area covered by Pt, and the computational results presented here are thus independent of the Pt thickness. The properties of the tandem photoabsorber and of the OER catalyst were the same as the values used in the calculations of $\eta_{STH,opt}$ for the uniform electrocatalyst films. The maximum $\eta_{STH,opt}$ of 25.0% was reached at f_c = 0.050, with a band-gap combination of 1.7 eV/1.1 eV for the top and bottom absorbers, respectively. When the filling fraction decreased below 0.010, a significant drop in $\eta_{STH,opt}$ was observed due to the rapid increase of the kinetic overpotential and the resulting high band-gap combinations required to drive the water-splitting reaction with such low filling-fraction films. For instance, at f_c = 0.0050, the optimal band-gap combination was 1.8 eV/1.2 eV, with $\eta_{STH,opt}$ (23.4%) primarily limited by the large band-gap values of the tandem photoabsorbers. As the filling fraction increased beyond f_c = 0.010, $\eta_{STH,opt}$ exhibited only a weak dependence on the filling fraction of the catalyst film. In this plateau region, the decrease of the photocurrent densities due to the increased obscuration of the illumination could be mostly compensated for by decreasing the band gaps of the tandem photoabsorbers that would be used in the optimal device design. The dotted curves show the value of $\eta_{STH,opt}$ at different filling fractions when the exchange-current density was fixed at 1 mA cm^{-2} but different values of a single Tafel slope, from 23 mV dec^{-1} to 180 mV dec^{-1}, were used for the HER electrocatalyst. As the Tafel slope decreased, the maximum $\eta_{STH,opt}$ value occurred at a lower filling fraction, because the optical absorption loss became the dominant factor as compared to the kinetic overpotential loss of the system. For instance, when the Tafel slope was 23 mV dec^{-1}, a monotonic decrease of $\eta_{STH,opt}$ was calculated as f_c increased. When no optical obscuration was considered but the experimentally determined *J*–*E* characteristic of a thick Pt film was nevertheless used, the maximum STH conversion efficiency, $\eta_{STH,max}$, was 26.7%. The maximum $\eta_{STH,opt}$ (25.0%) of the

patterned Pt electrocatalyst films approached this ideal case limit. For low filling fractions, for example $f_c < 0.010$, the transmission through the catalyst-covered region in the patterned electrode is expected to have minimal impact on the system efficiency.

The interdependency of the obscuration of light, the decrease of the kinetic overpotential and the change of the optimal band-gap combination of the photoabsorbers was further illustrated by analysis of the operating current density of the device. Fig. 4b shows the *J–E* relationships for a photocathode and a photoanode, each with $f_c = 0.10$ or $f_c = 0.001$. As the filling fraction of the patterned photocathode increased from 0.001 to 0.10, the optimal band-gap combination of the tandem photoabsorber changed from 1.9 eV/1.3 eV to 1.7 eV/1.0 eV. The decrease of the optimal band-gap values improved the attainable photocurrents from the tandem cell. As a result, although the light obscuration increased as f_c increased, $\eta_{STH,opt}$ increased from 20.8% to 24.4%.

Fig. 4c plots η_{STH} as a function of the filling fraction when fixed, experimentally obtained *J–E* relationships (see ESI†) for two characteristic multi-junction cells (a triple-junction a-Si cell and a triple-junction III–V cell)[13,14] were used instead of assuming that the light absorbers operated at the ideal Shockley–Queisser limit. The performance of the Pt electrocatalyst film in this study and the state-of-the-art OER catalyst were used in the calculation for the electrocatalyst properties on the top and the bottom side of the tandem structure, respectively. A similar trend to that depicted in Fig. 4a was observed using these actual performance parameters of existing light absorbers. Specifically, as the filling fraction of the patterned Pt film decreased below 0.010, a significant reduction of η_{STH} was observed due to the increase of the kinetic overpotentials, whereas a relatively small change in η_{STH} was observed as the filling fraction varied from $f_c = 0.010$ to 0.10, due to the trade-off between increased current as the obscuration decreased, and an increased overpotential producing a lower current at the operating point than that could optimally be obtained from these specific light absorbers.

A similar calculation was performed to evaluate the design rules for a situation in which the light was incident upon a photoanode having a patterned OER electrocatalyst, and a similar trend of the dependence of η_{STH} on the filling fraction was observed. Due to the poor adhesion between the Ir/IrO_x films and Si or FTO substrates and also due to the high $J_{catalyst}$ values at low filling fractions, the experimental *J–E* characteristics of IrO_x films at varied filling fractions was difficult to obtain. Fig. 4d shows the value of $\eta_{STH,opt}$ (dotted curves) as a function of the filling fraction when the Tafel slope of the IrO_x was systematically varied from 60 mV dec^{-1} to 240 dec^{-1}, for the use of a patterned IrO_x electrocatalyst on the top, light-facing, anode of a tandem-absorber device structure. However, the reaction mechanism and the resulting Tafel slope will likely be different at high current densities, as was observed experimentally for Pt (Fig. 2). The solid line in Fig. 4d illustrates the trend for $\eta_{STH,opt}$ when two Tafel slopes were employed, based on data reported previously for the OER.[15] Note that complete transmission and complete reflection/absorption were also assumed in the catalyst-free and catalyst-covered regions of the patterned OER electrode, respectively. In a design in which light is incident upon the OER-catalyst-bearing side of the photoanode, the optical properties of the catalyst, especially under working conditions that result in the formation of hydroxide/oxyhydroxide species, are different from that of the starting metal oxides and are certainly different from that of the metals used on the photocathode side of the structure. Therefore, the completely optically opaque catalyst assumed in the calculation represented the lower limit of the STH conversion efficiency in the patterned system for both photocathode-up and photoanode-up designs, without considering the optical properties of the catalysts in more detail.

IV. Discussion

A. Comparison between the STH conversion behavior of patterned and uniformly coated electrocatalyst films

In tandem photoabsorbers coated with uniform catalyst films, as the thickness of the catalyst film decreases, the integrated parasitic absorption decreases, but the kinetic overpotentials required to drive the reaction at the same $J_{electrode}$ often increase, which requires a change in the band-gap combination of the tandem photoabsorbers to produce the optimal STH efficiency from the device. Therefore, the optimal film thickness and the value of $\eta_{STH,opt}$ is highly dependent on the catalytic and optical properties of the catalyst films as well as on the current–voltage characteristics of the tandem photoabsorbers. In general, the parasitic absorption can also alter the transmitted illumination spectrum and can therefore significantly reduce the optimal efficiency of the tandem photoabsorber due to current-matching constraints. For instance, the optimal fuel-conversion efficiency can be significantly reduced due to the infrared absorption of a thin water layer.[16] For many earth-abundant electrocatalysts (such as NiO_x and CoO_x) that are highly absorbing during electrocatalysis, especially in nanoporous forms that result in large surface areas,[17–20] the STH conversion efficiencies of devices that use uniformly coated catalyst films are largely limited by the parasitic absorption of the catalyst. Therefore, in theoretical calculations the optimal catalyst loadings often occur at ultrathin (<1 nm) film thicknesses, for which the optical obscuration of the catalyst films is reduced.[17,21] For the electrodes that utilize uniformly coated catalyst films, improvement of the transparency of the electrocatalyst films, such as microstructuring porous Pt films,[22] is an effective strategy to increase the optimal loading of the electrocatalysts and hence increase the optimal STH conversion efficiency of the device.

For the patterned catalyst films evaluated herein, as the filling fraction decreased, a similar trade-off between the light obscuration and the electrocatalytic performance occurred. However, the deleterious effects of optical obscuration and of a change in the transmitted illumination spectrum were reduced at low filling fractions of the patterned electrocatalyst films. Moreover, as the filling fraction increased, the decrease in the operational current density due to the increase of the optical obscuration could be offset by a decrease in the optimal band-gap values of the

tandem photoabsorber, because the electrocatalytic performance improved at higher filling fractions. As a result, when the band gaps of the photoabsorbers were optimized for each value of f_c, a wide range of f_c values in the patterned Pt film allowed for construction of a system having $\eta_{STH,opt} > 24\%$. Analogous design strategies have been proposed and experimentally demonstrated qualitatively for nanoemitter solar cells,[23,24] for Si photoelectrodes patterned using nanosphere lithography,[25,26] and for fuel-forming reactions.[27,28]

B. Materials utilization for patterned electrocatalyst films

In acidic aqueous solutions, the state-of-the-art electrocatalysts for the HER and the OER contain noble metals and metal oxides, such as Pt and IrO_2, which operate at overpotentials of -55 mV and 270 mV at current densities of 10 mA cm^{-2} in magnitude for the HER and OER, respectively,[29] although recent work with transition-metal phosphides has shown overpotentials for the HER that approach that of Pt.[30–32] IrO_x is the only stable reported active OER electrocatalyst in acidic electrolytes.[8] The use of Pt or Ir as electrocatalysts in large-scale photoelectrolysis systems could be cost prohibitive and may not be viable based on the worldwide proven reserves or current world production of these elements. To obtain an estimate of the cumulative supply requirements for these materials, a photoelectrolysis system with an efficiency of 10% was assumed to achieve 10 TW peak power output. From the performance analysis of the patterned Pt film described in Fig. 2a, with the appropriate light absorbers, a 2 nm thick Pt film with $f_c = 0.010$ can readily achieve a target 10% STH efficiency. At $f_c = 0.010$, assuming no optical concentration, 4.4×10^4 kg of Pt would be required to meet a 10 TW_p target deployment level. This value is small compared to the current 6.6×10^7 kg of proven world reserves for Pt, and in 2012, the global production of Pt was 1.8×10^5 kg $year^{-1}$. At $f_c = 0.010$, the cost of 2 nm of Pt is ~ 0.017 \$ m^{-2}. In contrast, for an IrO_x coated photoanode with a loading of 10 g m^{-2} (typical PEM electrolyzer loading) and with $f_c = 0.010$, $\sim 10^7$ kg of Ir would be required to meet a 10 TW_p deployment level, as compared to the estimated 10^6 kg global resource base of Ir.[33]

C. Materials and system designs well-suited to exploit patterned electrocatalyst films

The patterned catalyst design has been proposed and experimentally implemented qualitatively previously for photocathodes.[23,24,27,28,34,35] In system designs that utilize planar absorber device structures, such as a louvered design[36] or a side-by-side design,[3] in which the HER catalyst or/and the OER catalyst are exposed to the solar illumination, the optical obscuration that accompanies the use of uniformly coated electrocatalyst films prevents the use of catalyst loadings that provide the lowest possible overpotentials from those specific materials. Patterning the catalyst films in low filling fractions is an effective strategy to minimize the parasitic absorption and to leverage highly absorbing catalyst films in such up-facing devices and system configurations. For electrocatalyst materials that are highly catalytically active at high operational current densities, and especially for electrocatalysts that have small Tafel slopes, the use of patterned electrocatalyst films is an effective strategy to achieve an optimal solar-to-fuel conversion efficiency, independent of the optical properties of the catalyst materials under operational conditions. This approach also minimizes the use of noble metals. For instance, due to the active HER catalysis of Pt, the patterning of HER photocathodes with low filling fractions of Pt in principle obviates the need for an earth-abundant substitute for the Pt HER electrocatalyst in planar, cathode-up implementations of various solar fuel-generating devices.

In 3-dimensional, microwire-based designs, such as the absorber-in-membrane design,[1,3] a high loading of optically opaque catalyst materials can be accommodated while incurring minimal parasitic absorption by placing the catalyst materials at the base of the microwire arrays.[37,38] Hence, in such designs, the STH conversion efficiency can be decoupled from the optical properties of the catalyst materials. However, to beneficially utilize an architecture that involves selective deposition of catalyst materials at the base of the structure, an emitter layer or other conductive film is required to transport photogenerated charge carriers to the catalyst films.

For materials assemblies that require additional adhesion layers between the catalyst and the photoabsorber, *e.g.*, Pt on Si photoelectrodes, or that require protection layers for stable solar-fuel operations, the adhesion layer and the protection layer would generally further increase the parasitic absorption of the system if proper dielectric antireflective strategies are not implemented. Therefore, in such systems, the patterned electrocatalyst approach is preferred relative to uniformly coated planar catalyst systems. The patterned electrocatalyst strategy is especially important for electrocatalysts that are highly absorbing/reflecting, and for electrocatalysts that are electrochromic under working conditions, specifically such as transition-metal oxide OER catalysts. Moreover, for catalysts that are not highly active and thus require increased loading on the light absorber, the patterning strategy allows for the use of thick and/or nanoporous electrocatalysts without producing a significant reduction in the optical absorption in the underlying light absorbers.

For semiconductor/electrolyte junctions with high barrier heights that provide effective charge separation at the photocathode or photoanode, use of a uniform catalyst coating often introduces deleterious interfacial states and consequently decreases the performance of the resulting solid/liquid junctions.[39] In contrast, patterned catalyst films that exploit ''pinch-off'' effects as well as radical collection of photogenerated charge carriers could retain a high effective barrier height relative to a planar catalyst system, in which the barrier height would be complicated and potentially lowered by the semiconductor/catalyst interface.[26] Optimization of the patterned catalyst design remains important in this case, considering the balance of optical absorption and the minority-carrier diffusion length as well as the resistivity of any inversion layer, to maximize the carrier-collection efficiency and minimize the series-resistance losses.

As a result of minimal light obscuration, the patterned electrocatalyst films with low filling fractions are well suited

for solar-fuels device designs that utilize non-imaging 1-dimensional or 2-dimensional solar concentrators. The operational current densities at the catalyst surface in the concentrator designs are likely to be 10 times higher than in flat-plate designs, at the same filling fraction of electrocatalyst in both types of systems. Therefore, electrocatalyst materials that are highly active at high operational current densities (1–2 A cm^{-2}), or nanoporous materials that could enable high catalyst loadings, would be beneficially used in such systems in the patterned design as opposed to in continuous film form. In contrast, due to the high operational current density, system designs such as vapor-feed PEC cells are more challenging to implement using low filling fraction patterned electrocatalyst films.

A constraint of the patterned electrocatalyst design is that photogenerated minority carriers obviously must be able to effectively reach the electrocatalyst. Hence, either a conductive layer (such as a transparent conducting oxide) is required on the absorber, or the electrocatalyst islands must be spaced on a pitch that does not significantly add resistance losses from the transparent conducting oxide or the minority-carrier collection length in the underlying absorber. Provided that this constraint is met, the approach should be applicable and advantageous for a variety of proposed and implemented photoelectrode devices and system designs, including side-by-side system designs, vertically integrated tandem-structure system designs, 1-D and 2-D nonimaging-concentrator system designs, as well as for devices based on microwire and nanowire arrays and other mesoscopic device morphologies.

We note that the comparisons described herein assume a trade-off between increased optical obscuration and increased catalytic activity, as a result of increasing the film thickness, but that all else is held constant. Other effects, including enhanced light scattering, enhanced surface area, and small radius-of-curvature for enhanced bubble formation/release especially on patterned nanoscale catalysts, can produce different outcomes, if they can be exploited favorably in an integrated photoelectrode structure with varying thicknesses of electrocatalyst films.

V. Conclusions

Patterning electrocatalysts on the surface of photoabsorbers in a solar-fuels generator provides a viable approach to minimize parasitic absorption of catalyst films, but involves operation at high current densities in the regions of the surface covered by the electrocatalyst. At very low filling fractions ($f_c < 0.010$), a further decrease in the filling fraction results in a significant decrease in the solar-to-hydrogen efficiency, $\eta_{STH,opt}$, of a system designed with the optimal band gaps to accommodate that specific coverage of electrocatalyst, because the increase of the kinetic overpotential overwhelms the reduction in the parasitic absorption. At low filling fractions ($0.010 < f_c < 0.10$), $\eta_{STH,opt}$ exhibited a weak dependence on the filling fraction of the electrocatalyst, because as the filling fraction increased, the reduction of the kinetic overpotential allowed the use of tandem photoabsorbers with smaller band-gap combinations, and thus yielded higher optimal operating current densities that compensated for the increase in the parasitic light absorption due to the electrocatalyst. Ultramicroelectrodes prepared by a lithographic lift-off process provided a robust analytical platform for investigating the intrinsic HER kinetics of metal electrocatalysts at extremely high current densities, and stable current densities as high as 10 A cm^{-2} were obtained with negligible concentration-overpotential losses associated with mass transport. Two distinct slopes of the current-density *versus* potential relationship for Pt ultramicroelectrode arrays, 23 mV dec^{-1} at low cathodic current densities (1 mA cm^{-2} to 10 mA cm^{-2}) and 180 mV dec^{-1} at high cathodic current densities (1 A cm^{-2} to 10 A cm^{-2}) were observed using patterned Pt electrocatalyst films. In conjunction with optimization of the band gaps of the light absorbers, designs that exploit low filling fractions of electrocatalysts on photoelectrodes can significantly reduce the usage of precious metals, such as Pt or Ir, by two orders of magnitude relative to uniform planar films, with only marginal decreases in the attainable values of $\eta_{STH,opt}$. The implementation of this design strategy is preferred in materials assemblies that require opaque adhesion layers or protection layers between the photoabsorbers and the electrocatalysts, as well as in mixed semiconductor/electrolyte and semiconductor/metal junctions that leverage "pinch-off" effects.

Acknowledgements

This material is based upon work performed by the Joint Center for Artificial Photosynthesis, a DOE Energy Innovation Hub, supported through the Office of Science of the U.S. Department of Energy under Award Number DE-SC0004993. UV-VIS spectroscopy and AFM were performed at the Beckman Institute Molecular Materials Resource Center (MMRC) at the California Institute of Technology. We also thank E. Warren for stimulating discussions, Z. Huang for assistance with the AFM measurement and K. Papadantonakis for assistance on the editing of this manuscript.

References

1 M. G. Walter, E. L. Warren, J. R. McKone, S. W. Boettcher, Q. Mi, E. A. Santori and N. S. Lewis, *Chem. Rev.*, 2010, **110**, 6446–6473.
2 S. Haussener, S. Hu, C. Xiang, A. Z. Weber and N. Lewis, *Energy Environ. Sci.*, 2013, **6**, 3605–3618.
3 S. Haussener, C. X. Xiang, J. M. Spurgeon, S. Ardo, N. S. Lewis and A. Z. Weber, *Energy Environ. Sci.*, 2012, **5**, 9922–9935.
4 S. S. Mao and S. Shen, *Nat. Photonics*, 2013, **7**, 944–946.
5 C. Xiang, Y. Chen and N. S. Lewis, *Energy Environ. Sci.*, 2013, **6**, 3713–3721.
6 K. Sun, S. Shen, Y. Liang, P. E. Burrows, S. S. Mao and D. Wang, *Chem. Rev.*, 2014, **114**, 8662–8719.
7 L. Trotochaud, T. J. Mills and S. W. Boettcher, *J. Phys. Chem. Lett.*, 2013, **4**, 931–935.

8 C. C. L. McCrory, S. H. Jung, J. C. Peters and T. F. Jaramillo, *J. Am. Chem. Soc.*, 2013, **135**, 16977–16987.
9 S. W. Boettcher, E. L. Warren, M. C. Putnam, E. A. Santori, D. Turner-Evans, M. D. Kelzenberg, M. G. Walter, J. R. McKone, B. S. Brunschwig, H. A. Atwater and N. S. Lewis, *J. Am. Chem. Soc.*, 2011, **133**, 1216–1219.
10 S. A. Vilekar, I. Fishtik and R. Datta, *J. Electrochem. Soc.*, 2010, **157**, B1040–B1050.
11 A. J. Bard and L. R. Faulkner, *Electrochemical Methods, Fundamentals and Applications*, Wiley, 2000.
12 R. M. Penner and C. R. Martin, *Anal. Chem.*, 1987, **59**, 2625–2630.
13 H. Cotal, C. Fetzer, J. Boisvert, G. Kinsey, R. King, P. Hebert, H. Yoon and N. Karam, *Energy Environ. Sci.*, 2009, **2**, 174–192.
14 K. Beernink, S. Guha, J. Yang, A. Banerjee, K. Lord, G. DeMaggio, F. Liu, G. Pietka, T. Johnson, M. Reinhout, K. Younan and D. Wolf, *Lightweight, Flexible Solar Cells on Stainless Steel Foil and Polymer for Space and Stratospheric Applications*, Brook Park, Ohio, 2005.
15 J.-M. Hu, J.-Q. Zhang and C.-N. Cao, *Int. J. Hydrogen Energy*, 2004, **29**, 791–797.
16 H. Doscher, J. F. Geisz, T. G. Deutsch and J. A. Turner, *Energy Environ. Sci.*, 2014, **7**, 2951–2956.
17 L. Trotochaud, T. J. Mills and S. W. Boettcher, *J. Phys. Chem. Lett.*, 2013, **4**, 931–935.
18 J. M. Gregoire, C. Xiang, S. Mitrovic, X. Liu, M. Marcin, E. W. Cornell, J. Fan and J. Jin, *J. Electrochem. Soc.*, 2013, **160**, F337–F342.
19 F. Švegl, B. Orel, M. G. Hutchins and K. Kalcher, *J. Electrochem. Soc.*, 1996, **143**, 1532–1539.
20 B. Orel, M. Macek, F. Svegl and K. Kalcher, *Thin Solid Films*, 1994, **246**, 131–142.
21 A. Shinde, D. Guevarra, J. A. Haber, J. Jin and J. M. Gregoire, *J. Mater. Res.*, 2014, **30**, 442–450.
22 A. Heller, D. E. Aspnes, J. D. Porter, T. T. Sheng and R. G. Vadimsky, *J. Phys. Chem.*, 1985, **89**, 4444–4452.
23 A. G. Muñoz and H. J. Lewerenz, *ChemPhysChem*, 2010, **11**, 1603–1615.
24 T. Stempel, M. Aggour, K. Skorupska, A. Muñoz and H.-J. Lewerenz, *Electrochem. Commun.*, 2008, **10**, 1184–1186.
25 R. C. Rossi, M. X. Tan and N. S. Lewis, *Appl. Phys. Lett.*, 2000, **77**, 2698–2700.
26 R. C. Rossi and N. S. Lewis, *J. Phys. Chem. B*, 2001, **105**, 12303–12318.
27 D. V. Esposito, I. Levin, T. P. Moffat and A. A. Talin, *Nat. Mater.*, 2013, **12**, 562–568.
28 L. Ji, M. D. McDaniel, S. Wang, A. B. Posadas, X. Li, H. Huang, J. C. Lee, A. A. Demkov, A. J. Bard, J. G. Ekerdt and E. T. Yu, *Nat. Nanotechnol.*, 2015, **10**, 84–90.
29 S. Trasatti, *J. Electroanal. Chem. Interfacial Electrochem.*, 1972, **39**, 163–184.
30 J. F. Callejas, J. M. McEnaney, C. G. Read, J. C. Crompton, A. J. Biacchi, E. J. Popczun, T. R. Gordon, N. S. Lewis and R. E. Schaak, *ACS Nano*, 2014, **8**, 11101–11107.
31 J. M. McEnaney, J. C. Crompton, J. F. Callejas, E. J. Popczun, A. J. Biacchi, N. S. Lewis and R. E. Schaak, *Chem. Mater.*, 2014, **26**, 4826–4831.
32 E. J. Popczun, J. R. McKone, C. G. Read, A. J. Biacchi, A. M. Wiltrout, N. S. Lewis and R. E. Schaak, *J. Am. Chem. Soc.*, 2013, **135**, 9267–9270.
33 M. L. Zientek, J. D. Causey, H. L. Parks and R. J. Miller, Platinum-Group Elements in Southern Africa—Mineral Inventory and an Assessment of Undiscovered Mineral Resources, 2005, U.S. Geological Survey Scientific Investigations Report 2010-5090-Q, p. 126 and GIS data, http://dx.doi.org/10.3133/sir20105090Q.
34 M. Lublow, B. Bouabadi and S. Kubala, *Sol. Energy Mater. Sol. Cells*, 2012, **107**, 56–62.
35 K. T. Fountaine, H. J. Lewerenz and H. A. Atwater, *Appl. Phys. Lett.*, 2014, **105**, 173901.
36 K. Walczak, Y. Chen, C. Karp, J. W. Beeman, M. Shaner, J. Spurgeon, I. D. Sharp, X. Amashukeli, W. West, J. Jin, N. S. Lewis and C. Xiang, *ChemSusChem*, 2015, **8**, 544–551.
37 J. R. McKone, E. L. Warren, M. J. Bierman, S. W. Boettcher, B. S. Brunschwig, N. S. Lewis and H. B. Gray, *Energy Environ. Sci.*, 2011, **4**, 3573–3583.
38 E. L. Warren, J. R. McKone, H. A. Atwater, H. B. Gray and N. S. Lewis, *Energy Environ. Sci.*, 2012, **5**, 9653–9661.
39 A. J. Nozik and R. Memming, *J. Phys. Chem.*, 1996, **100**, 13061–13078.